Proceedings of the 11th ICPMG 2026
11th International Conference on Physical Modelling in Geotechnics
8-12 June 2026, Zurich, Switzerland

Influence of bubble seepage on methane gas production and pore pressure evolution during hydrate dissociation in marine sediments

Peng Wang, Lujun Wang, Zhigang Ye, Bin Zhu, Yunmin Chen
Center for Hypergravity Experimental and Interdisciplinary Research, Zhejiang University, Hangzhou, 310058, PR China, 12012041@zju.edu.cn, lujunwang@zju.edu.cn, zhigangye@zju.edu.cn, binzhu@zju.edu.cn, chenyunmin@zju.edu.cn.

ABSTRACT: Natural gas hydrates are widely distributed in marine sediments and are considered as a promising unconventional energy resource. The characterization of liquid-gas flow during hydrate dissociation plays a critical role in assessing both the hydrate exploitation efficiency and the reservoir geomechanical responses. In this work, the gas seepage in the forms of isolated bubbles, connected gas, their combinations, and the transitions among them were governed by a newly proposed gas relative permeability function. A multi-phase and multi-field coupled model was accordingly developed and validated based on existing unit tests of gas percolation and hydrate deposit dissociation. Following, the impacts of isolated bubble seepage during hydrate dissociation were preliminarily investigated. Results indicate that the isolated methane gas bubbles delayed the occurrence of peak gas production rate and facilitated the localized excess pore pressure accumulation during the initial stage of hydrate dissociation. Upon reaching the critical gas saturation, the gas phase started to evolve from isolated bubbles to connected gas, leading to a sharp increase in gas relative permeability and a rapid release of accumulated gas. This model provides a theoretical basis and numerical method for evaluating the gas migration under extremely low gas saturation, as well as the exploitation of marine hydrate deposits.

1 INTRODUCTION

Marine sediments usually contain biogenic or thermogenic gases in nature, such as methane (CH_4), carbon dioxide (CO_2), and hydrogen sulfide (H_2S), either dissolved in pore water or as free gas phase (Floodgate and Judd, 1992). Gassy sediments are typically maintained at high water saturation, generally exceeding 85% (Sultan and Garziglia, 2014).

For methane gas trapped in the hydrate form, which is a solid compound of methane and water molecules at high pressure and low temperature conditions (Sloan, 2003), the global mass of carbon in hydrates ranges from 3 to 455 Gt (Boswell and Collett, 2011; Milkov, 2004; Piñero et al., 2013). This is comparable to the total carbon content of proven reserves of petroleum and natural gas worldwide(Parker and Mainelli, 2024).

During gas production from the hydrate deposits, the gas saturation usually remains below 30% due to continuous gas generation from hydrate dissociation and supplemental water influx from surrounding formations (P Wang et al., 2025; Ye et al., 2022). Under such low gas saturation conditions, the gas phase exists as a discontinuous, non-wetting phase trapped within pores, and the bubble morphology is controlled by pore structure (Floodgate and Judd, 1992; Sills and Wheeler, 1992). Accurate characterization of isolated bubble seepage behavior is therefore crucial for understanding subsea methane migration and optimizing gas production from natural gas hydrate reservoirs.

The centrifuge modelling and visualized tests of gas recovery from hydrate-bearing sediments reveal that the gas seepage under low gas saturation conditions can lead to pore pressure accumulation and soil skeleton deformation (L Wang et al., 2024; P Wang et al., 2025). However, for the numerical evaluations of gas migration in hydrate-bearing sediments, conventional seepage models have been established based on the assumption of a connected gas phase (Figure 1a), and are difficult to accurately characterize gas seepage and production processes under low gas saturation conditions in hydrate-bearing sediments (Dai et al., 2012; Ito et al., 2015; Oshima et al., 2019; Santamarina et al., 2015). This limitation becomes particularly pronounced given the complex multi-field coupling effects and phase transition processes during hydrate dissociation (Sánchez et al., 2018), making the significant challenge for accurate simulation and evaluation of gas hydrate exploitation

and methane gas migration (Yamamoto et al., 2019). Characterizing gas seepage under low saturation conditions remains a critical unresolved issue.

This work introduces a novel bubble seepage model that explicitly accounts for the migration of isolated bubbles and their transition to a connected gas phase (Figure 1b). The model was validated based on a dissociation experiment of the field hydrate deposit pressure core. Then, the bubble seepage model's parameter sensitivity is discussed. This model provides a modified numerical approach for accurately characterizing gas seepage under low gas saturation conditions, thereby offering theoretical support for understanding marine gas migration and optimizing hydrate exploitation strategies.

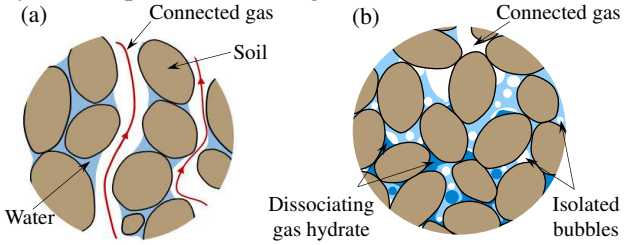

Figure 1. Diaphragm of fluid seepage within the pore space of marine sediments. (a) Seepage under the gas-connected hypothesis, and (b) seepage considering the transition from isolated bubbles to a connected gas phase.

2 MODEL DESCRIPTION

The improved Thermo-Hydro-Chemo-Mechanical coupled responses of hydrate-bearing sediments more systematically consider the evaporation/condensation process of water, the dissolution/exsolution process of gas, and the formation/dissociation process of hydrate in the mass conservation equations and energy conservation equation. Besides, the seepage process of connected gas, isolated bubbles, and their transformation is considered. The numerical model was established based on following assumptions: (a) The displacement of the solid skeleton is much smaller than its own geometric scale and the hydrates move together with soil skeleton, (b) solid is incompressible, (c) the liquid-gas seepage and gas diffusion obey Darcy's law and Fick's law, (d) energy transfer includes heat conduction and heat convection.

2.1 Mass conservation equations of fluids

The mass conservation equations for water and methane gas are expressed as (Teymouri et al., 2020):

$$\frac{\partial}{\partial t}\left[\varphi\left(\rho_g^w S_g+\rho_l^w S_l+\rho_h^w S_h\right)\right]+ \nabla\cdot\left(\mathbf{J}_g^w+\mathbf{J}_l^w+\rho_h^w S_h\varphi\mathbf{v}\right)=f_e^w \quad (1)$$

$$\frac{\partial}{\partial t}\left[\varphi\left(\rho_g^m S_g+\rho_l^m S_l+\rho_h^m S_h\right)\right]+ \nabla\cdot\left(\mathbf{J}_g^m+\mathbf{J}_l^m+\rho_h^m S_h\varphi\mathbf{v}\right)=f_e^m \quad (2)$$

where w and m denote water and methane respectively, s, h, l, and g denote solid, hydrate, liquid and gas respectively, φ is the porosity of host sediments, ρ_j^i (i = w, m, and j =s, h, l, g) is the mass of substance i in per unit volume of phase j, S_j is the saturation of phase j, $\mathbf{J}_j^i$ is the relative motion flux of substance i in the phase j to the solid phase. $\mathbf{v}$ is the solid velocity, f_e^i is the mass sink/source term of substance i.

2.2 Energy conservation equation

The equation for energy conservation, taking into consideration internal energy per unit volume and transport through the phases, is expressed as (Olivella et al., 1996):

$$\frac{\partial}{\partial t}\left\{\begin{array}{c}\left[e_s\rho_s(1\text{-}\varphi)\right]+\\ \varphi\left(e_g\rho_g S_g+e_l\rho_l S_l+e_h\rho_h S_h\right)\end{array}\right\}+ \nabla\cdot\left[\mathbf{J}_c+\left(\mathbf{J}_{El}+\mathbf{J}_{Eg}+\mathbf{J}_{Eh}+\mathbf{J}_{Es}\right)\right]=f^E \quad (3)$$

$$\mathbf{J}_c=-\left[(1-\varphi)\lambda_s+\varphi S_l\lambda_l+\varphi S_g\lambda_g+\varphi S_h\lambda_h\right]\nabla T \quad (4)$$

where ρ_j is the density of phase j, e_j is the specific internal energy per unit mass of phase j, which is elaborated in Table 1, $\mathbf{J}_c$ is the conductive heat flux, $\mathbf{J}_{Ej}$ is the advective energy flux of phase j, f^E is the energy sink/source term, λ_j is the heat conductivity tensor of phase j, T is the temperature.

Table 1. Specific energy of different substances in different phases

Substances and phases	equations
Sediments	$e_s=C_s\,(T-T_0)$
Hydrate	$e_h=H_{diss}+C_h\,(T-T_0)$
Liquid water	$e_w=C_w\,(T-T_0)$
Vapor	$e_{gw}=H_{evap}+C_{gw}\,(T-T_0)$
Gas	$e_m=C_m\,(T-T_0)$

*where C is heat capacity.

2.3 Momentum balance equation

The momentum conservation equation can be reduced to the equilibrium equation in the absence of inertial forces as follows (Sánchez et al., 2018):

$$\nabla\cdot\boldsymbol{\sigma}+\left[(1-\varphi)\rho_s+\varphi\left(\rho_g S_g+\rho_l S_l+\rho_h S_h\right)\right]\mathbf{g}=0 \quad (5)$$

$$\boldsymbol{\sigma}=\boldsymbol{\sigma}'-\alpha\mathbf{m}^T\left(S_l p_l+S_g p_g\right) \quad (6)$$

$$d\boldsymbol{\sigma}'=D_e(d\varepsilon-d\varepsilon_0-d\varepsilon^T) \quad (7)$$

where $\mathbf{g}$ is the gravitational acceleration vector, $\boldsymbol{\sigma}$ and $\boldsymbol{\sigma}'$ are the total stress and effective stress tensors, respectively, α is the Biot coefficient, $\mathbf{m}^T$ is a unit tensor (enabling the tensorial representation of the scalar term ($S_l p_l$ + $S_l p_l$)), p_l and p_g are liquid and gas

pressure, respectively, $d\varepsilon$, $d\varepsilon_0$, and $d\varepsilon^T$ are the total strain increment, non-stress induced strain increment (e.g., creep strain, assuming this term is 0 in this work), and thermo-induced strain increment, respectively, D_e is the elastic stiffness matrix, which is determined by the Poisson ratio v and elastic modulus E.

In the elastic constitutive relationship hypothesis in this work, the influence of hydrate saturation elastic modulus can be calculated by(Teymouri et al., 2020):

$$E=\left[E_s+dE_s\left(\varphi-\varphi_0\right)\right]\left(\frac{\sigma_c}{\sigma_{c0}}\right)^{b_E}+c_hE_hS_h^{d_E} \tag{8}$$

where E_s and E_h are the elastic moduli of hydrate-free sediments and bulk hydrate, respectively, φ_0 is the initial porosity at initial confining stress σ_{c0}, σ_c is the present confining stress, c_h is the contributional coefficient of hydrate to the elastic modulus of hydrate-bearing sediments, b_E and d_E are the stress level and hydrate saturation sensitivities of the elastic modulus, respectively.

2.4 Hydrate dissociation kinetics

Whether hydrates can stably exist in solid form can be characterized by the position of the phase equilibrium boundary and the current temperature and pressure state of the system. At a certain temperature T, if the environmental pressure p is greater than the phase equilibrium pressure of the hydrate, water and gas (such as carbon dioxide and methane) will form solid hydrates. If the environmental pressure drops below the phase equilibrium pressure of the hydrate p_{eq}, the hydrate will decompose and produce water and gas. The phase equilibrium boundaries of methane (CH_4) hydrate and carbon dioxide (CO_2) hydrate are expressed by Equations (9) and (10), respectively.

For methane hydrate (Ruan et al., 2012):

$$p_{eq}=1.15\exp\left(49.3185-\frac{9459}{T}\right) \tag{9}$$

For carbon dioxide hydrate (R Sun and Duan, 2005):

$$p_{eq}=20.95\exp(0.03977*T) \quad (255\text{K}<T\leq 272.6\text{K}) \tag{10a}$$

$$p_{eq}=3.703\exp(0.1306*T) \quad (272.6\text{K}<T\leq 282\text{K}) \tag{10b}$$

$$p_{eq}=55875.43*T^3-4.692*10^7*T^2+1.314*10^{10}*T-1.227*10^{12} \quad (283\text{K}<T\leq 293\text{K}) \tag{10c}$$

When the environmental pressure is lower than the hydrate phase equilibrium pressure p_{eq}, the hydrate dissociation rate can be described by the Kim-Bishnoi kinetic model, which is summarized based on the pure methane hydrate decomposition tests. The hydrate dissociation rate R_r is determined by the hydrate kinetic dissociation coefficient K_d, the specific surface area A_s of the hydrate, and the fugacity difference ($f_{eq}-f$) between the hydrate phase equilibrium state and the current state, as shown in Equation (11) (Kim et al., 1987):

$$R_r=K_dA_s\left(f_{eq}-f\right) \tag{11}$$

The fugacity difference is difficult to assess and is usually approximated by the difference between the environmental pressure and the hydrate phase equilibrium pressure ($p_{eq}-p$). The kinetic dissociation coefficient K_d is mainly determined by the kinetic dissociation constant K_{d0}, the phase transition activation energy ΔE, the ideal gas constant R, and the environmental temperature T (Equation 12):

$$K_d=K_{d0}\exp\left(-\frac{\Delta E}{RT}\right) \tag{12}$$

2.5 Fluid seepage and bubble migration

The liquid and gas advective seepage in porous media and the non-advective diffusion of gases (methane gas and water vapor) are commonly described by Fick's law and Darcy's law, respectively (X Sun et al., 2019).

$$I_g^i=\rho_g\frac{M_mM_w}{M_g^2}D_g^i\nabla\left(\frac{p_{gi}}{p_g}\right) \tag{13}$$

$$q_j=\frac{Kk_{rj}}{\mu_j}\left(-\nabla p_j+\rho_j\mathbf{g}\right) \tag{14}$$

where K is the intrinsic permeability of porous media, k_{rj} is the relative permeability of gas and liquid phases, μ_j is the viscosity of liquid and gas phases, D_g^i is the diffusion tensor of gas molecules, M_m, and M_w are the molar mass of methane and vapor, respectively. M_g is the weighted molar mass of the gas phase, which is calculated by:

$$\frac{1}{M_g}=\frac{\rho_g^w}{\rho_g}\frac{1}{M_w}+\frac{\rho_g^m}{\rho_g}\frac{1}{M_m} \tag{15}$$

The gas partial pressure p_{gi} and ρ_{ji} of substance i in the gas phase are respectively determined according to Dalton's partial pressure law (Equation 16) and the Clapeyron equation (Equation 17).

$$p_g=\sum_{i=w,m}p_{gi} \tag{16}$$

$$\rho_g^i=\frac{p_{gi}M_i}{RT} \tag{17}$$

The intrinsic permeability K of hydrate-bearing sediments decreases with increasing hydrate saturation (X Sun et al., 2019).

$$K=K_0\left(\frac{\varphi}{\varphi_0}\right)^{1.5}\left(\frac{1-\varphi}{1-\varphi_0}\right)^3(1-S_h)^{n_k} \tag{18}$$

where K_0 is the intrinsic permeability of hydrate-free sediments, n_k is a hydrate morphology-related index.

The capillary pressure p_c is described by the Brooks-Corey soil water retention curve.

$$p_c=p_g-p_l=p_0\left[\frac{S_l/\left(S_l+S_g\right)-S_{rl}-S_{rg}}{1-S_{rl}-S_{rg}}\right]^{-n_c} \tag{19}$$

Where p_0 is the gas entry pressure, n_c is the pore structure-related index.

The Corey model is widely adopted for describing the relative permeability of two-phase flow (e.g., liquid and gas) in porous media. It postulates that both phases are geometrically continuous and the flow follows Darcy's law (Ye et al., 2022).

$$k_{rcj}=\left(\frac{S_j - S_{rj}}{1 - S_{rj}}\right)^{n_j} \tag{20}$$

where S_{rj} represents the residual saturation of liquid and gas; n_j is the relative permeability characteristic index, which is related to the pore shape and pore network of the porous medium.

The bubble seepage function k_{rg} for hydrate-bearing sediments was proposed by modifying the commonly used relative gas permeability function with the connected-gas hypothesis k_{rgc} to consider the influence of hydrate saturation, isolated bubbles, and the transition from isolated bubbles to connected gas(Hu et al., 2024; van der Meer et al., 2018).

$$k_{rg}=\frac{k_{rgc}}{1+R_g F_g} \tag{21}$$

The parameter R_g is a variable that accounts for the maximum flow resistance of the isolated bubble within the sediment's pore space. Higher R_g corresponds to a lower gas relative permeability at low gas saturation conditions.

$$R_g=\frac{R_{g0}\mu_l\rho_l}{\varphi}\exp\left(\frac{1}{1 - S_h}\right) \tag{22}$$

The parameter F_g describes the dependency of the bubble strength on both gas saturation and sediment porosity.

$$F_g=0.5+\frac{arctan\left[\kappa\left(\theta^* - \varphi S_g\right)\right]}{\pi} \tag{23}$$

where κ is a positive parameter that controls the width of the transition band between isolated bubbles and connected gas, θ^* denotes the limiting gas amount when bubbles begin to transit into connected gas.

Figure 2 shows the variation of relative gas permeability with gas saturation for both the commonly used seepage function (Equation 20) and the modified bubble seepage function (Equation 21). The model predictions are further compared with previous experimental data and pore network modeling results (Johnson et al., 2011; Mahabadi et al., 2016). For conventional liquid-gas seepage models based on the connected-gas hypothesis, the relative gas permeability remains relatively high even at low gas saturations. In contrast, the bubble seepage function accounts for the extremely low relative permeability of isolated gas bubbles under low gas saturation conditions. In this state, the migration of gas bubbles is primarily driven by liquid seepage. Once the gas saturation reaches a critical threshold corresponding to the volumetric fraction of the gas phase, isolated bubbles begin to coalesce and transition into a connected gas phase, resulting in a rapid increase in relative gas permeability.

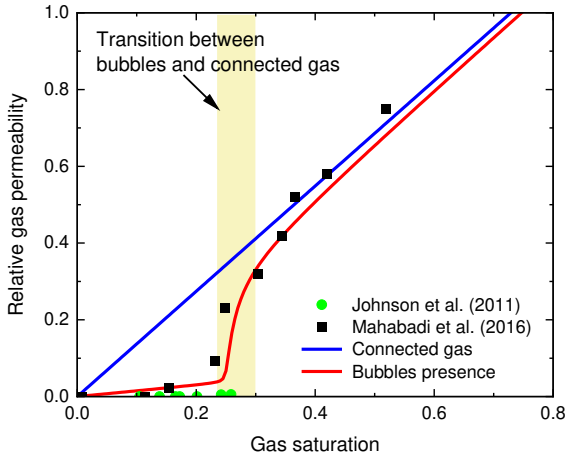

Figure 2. Comparison of relative gas permeability variation between different relative seepage functions. The blue curve is the commonly used relative gas permeability function, and the red curve is a modified bubble seepage function.

3 NUMERICAL CALCULATION AND VERIFICATION

3.1 Model calculation

The governing equations are numerically calculated on an open source finite element platform OpenGeoSys-6 (OGS-6) (Kolditz et al., 2012). Shape functions and weight functions are introduced to correlate the four partial differential equations (Eqs. 1, 2, 3, and 5) with the four primary variables $[p_g, p_l, T, u]^T$. The model is spatially discretized using the finite element method and temporally discretized using the backward Euler finite difference method. After establishing the Jacobian matrix, the Newton-Raphson method is employed to iteratively solve the nonlinear equation system (Equation 24) in a fully coupled manner.

Compared to conventional approaches that characterize hydrate phase change processes through source/sink terms in the liquid-gas mass conservation and energy conservation equations, this study establishes mass conservation equations based on the water and gas components within the solid (water and gas in hydrate), liquid (water and dissolved gas), and gas (methane/carbon dioxide and water vapor) phases. The system's energy conservation is described using specific energy forms (sensible heat of substances and latent heat of phase change). This formulation significantly reduces the additional computational load caused by frequent mass exchange and enthalpy changes during phase transitions, such as water

evaporation-condensation, gas dissolution-exsolution, and hydrate dissociation-secondary formation.

$$\begin{bmatrix} M_{gg} & M_{gl} & M_{gT} & M_{gu} \\ M_{lg} & M_{ll} & M_{lT} & M_{lu} \\ M_{Tg} & M_{Tl} & M_{TT} & M_{Tu} \\ 0 & 0 & 0 & 0 \end{bmatrix} \frac{\partial}{\partial t} \begin{bmatrix} \bar{p}_g \\ \bar{p}_l \\ \bar{T} \\ \bar{u} \end{bmatrix} + \begin{bmatrix} K_{gg} & K_{gl} & K_{gT} & 0 \\ K_{lg} & K_{ll} & K_{lT} & 0 \\ K_{Tg} & K_{Tl} & K_{TT} & 0 \\ K_{ug} & K_{ul} & K_{uT} & K_{uu} \end{bmatrix} \begin{bmatrix} \bar{p}_g \\ \bar{p}_l \\ \bar{T} \\ \bar{u} \end{bmatrix} = \begin{bmatrix} f_g \\ f_l \\ f_T \\ f_u \end{bmatrix} \quad (24)$$

3.2 Model verification

To validate the model's accuracy in simulating gas seepage processes during the dissociation of hydrate-bearing sediments, a geometric model was established based on existing hydrate depressurization dissociation experiments, which utilized a pressure core sample from the Ulleung Basin in the Sea of Japan (East Sea) (Yun et al., 2011). Numerical boundary conditions were configured accordingly. The specific gravity, clay content, liquid limit, plastic limit, and plastic index of the host sediment are 2.57, 12%, 115, 65, and 50, respectively. The undrained shear strength of hydrate-bearing sediments is about 286 kPa. As shown in Figure 3a, the geometric model represents a cylindrical pressure core with a diameter of 50 mm and a height of 822 mm. Temperature and pressure monitoring points were set at the 400 mm height of the model to track changes in temperature and pressure within the hydrate deposit during depressurization-induced dissociation. The model initial porosity φ_0 = 0.75, and the initial pore space hydrate saturation in the sediment is 19.5% for the hydration number χ = 5.99.

As shown in Figures 3b and 3c, when the bubble seepage model was applied, the rate of pressure decreased significantly and slowed. This is because gas release from hydrate dissociation occurred as the pressure core was depressurized to the hydrate phase equilibrium boundary. During this period, the model temperature dropped rapidly from approximately 277 K to about 274 K as a result of the endothermic hydrate dissociation, and this temperature is close to the hydrate phase equilibrium temperature at the prevailing pressure. As illustrated in Figure 3d, the bubble seepage model effectively captured the experimentally observed lag between hydrate dissociation and gas production. This phenomenon is attributed to the entrapment of gas in the form of isolated bubbles within the sediment due to low relative permeability.

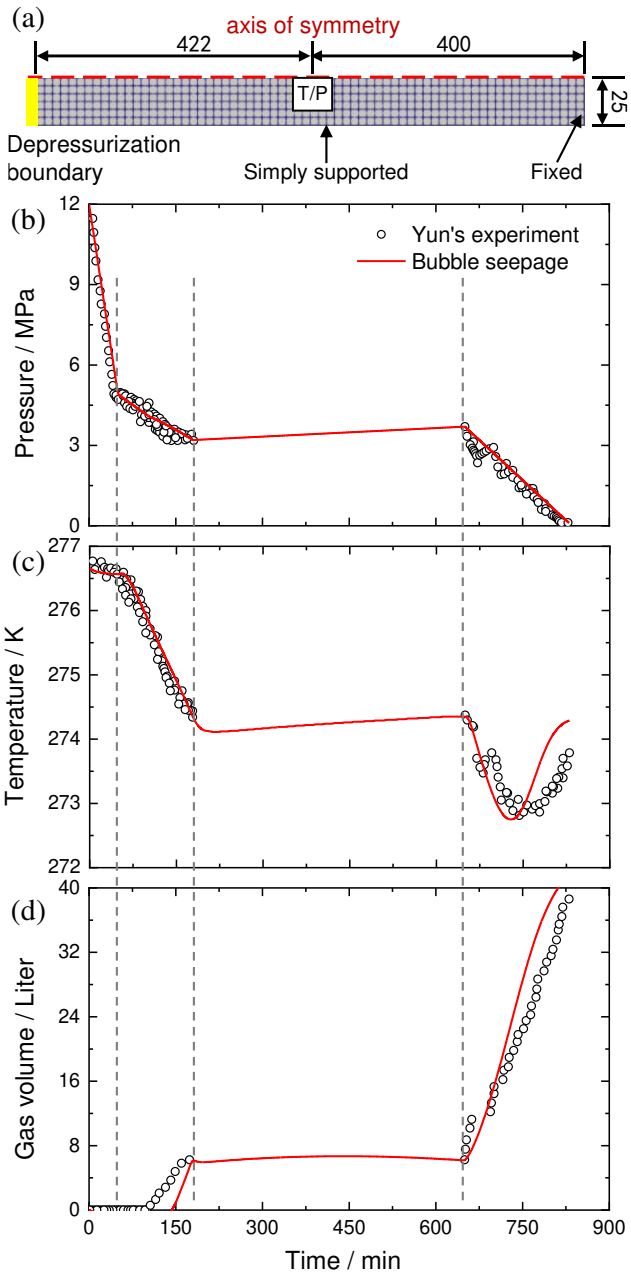

Figure 3. Model verification based on the dissociation experiment of the pressure core from the Ulleung Basin in the Sea of Japan (East Sea). (a) geometric model description. Comparisons between numerical and experimental results: (b) pressure, (c) temperature, and (d) gas production volume (unit: mm).

The depressurization boundary was then closed, maintaining the system in a sealed state for 8 hours (from t = 180 min to t = 650 min). During this period, heat transfer across the boundary led to a slight increase in model temperature. Concurrently, gas generation from continued hydrate dissociation and thermal expansion of the gas phase due to temperature rise caused the model pressure to increase, following the corresponding phase equilibrium pressure. At t = 650 min, depressurization was resumed to completely dissociate the remaining hydrate. The discrepancies

between the numerical results and experimental measurements during this period are attributed to the fluctuations in the depressurization boundary pressure and the heterogeneous distribution of hydrate in the experimental system.

4 RESULTS AND DISCUSSIONS

The depressurization experiments on hydrate-bearing sediments that conducted by Masuda. (1999) are widely recognized in the development and validation of numerical models for hydrate-bearing sediments, and have frequently served as benchmark cases for numerical verification and comparative studies (Masuda, 1999). This work also adopts this well-established experimental case to facilitate direct comparison and cross-validation of our numerical results with those from other existing numerical models.

Figure 4a presents the geometric model established based on the experimental conditions and boundary configurations. The pressure core model has a diameter of 51 mm and a height of 300 mm, with an initial porosity $\varphi_0 = 0.182$, representing a typical low-permeability hydrate-bearing sediment pressure core. The initial saturations of water, gas, and hydrate within the model pore space are $S_l = 0.443$, $S_g = 0.206$, and $S_h = 0.351$, respectively.

Figure 4b shows the experimental and numerical results of pressure variation at the bottom monitoring point P during hydrate dissociation. The conventional connected gas seepage model, constrained by its high gas relative permeability under low gas saturation and the extremely low intrinsic permeability resulting from high hydrate saturation in low porosity sediments, captures only the slowdown of pore pressure decrease following the onset of hydrate dissociation. In contrast, the bubble seepage model obviously reproduces the pore pressure increase caused by the impeded migration of isolated gas bubbles, as well as the subsequent pressure drop when these isolated bubbles transform into a connected gas phase with higher seepage mobility. However, the conventional gas relative permeability model fails to adequately capture these phenomena. These results demonstrate the distinct advantage of the proposed bubble seepage model in characterizing seepage behavior under low gas saturation conditions, particularly in reservoirs with low intrinsic permeability.

To investigate the impact of the low mobility of isolated gas on gas production behavior during hydrate dissociation in water-saturated and low-permeability reservoirs, the analysis of pore pressure evolution and gas production rate was conducted based on the geometric model shown in Figure 4a, focusing on the depressurization-induced dissociation process in fully water-saturated hydrate-bearing sediments (initial gas saturation $S_g = 0$).

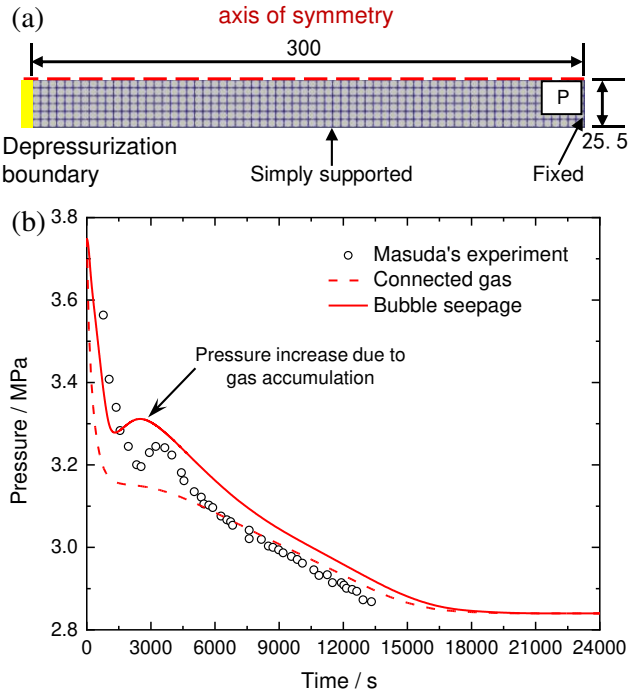

Figure 4. Impact of different relative gas permeability models on pore pressure evolution during hydrate dissociation and comparison with Masuda's experimental result. (a)geometric model description, and (b) pressure variation (unit: mm).

As shown in Figure 5a, under water-saturated conditions, the pressure accumulation caused by gas entrapment occurs at approximately 3.5 MPa, which is significantly higher than the value of 3.3 MPa observed under unsaturated conditions (Figure 4b). This difference can be attributed to the higher gas bubble mobility in unsaturated sediments, which allows a portion of the dissociated gas to be released during depressurization, thereby mitigating the pore pressure accumulation induced by isolated bubbles. In contrast, within water-saturated hydrate-bearing sediments, the gas generated during the initial dissociation stage is quantitatively trapped within pore space, leading to more pronounced pore pressure accumulation. Furthermore, a higher flow resistance of isolated bubbles results in more significant pore pressure accumulation during hydrate dissociation.

Figures 5b and c show that while the total gas production volume remains unchanged when using the bubble seepage model, a stronger bubble flow resistance prolongs the time required for complete hydrate dissociation. A delayed peak in gas production rate and a reduction in its magnitude are also observed.

This delay occurs because the internal pore pressure accumulation effectively decreases the hydrate dissociation rate, thereby slowing the overall gas production process.

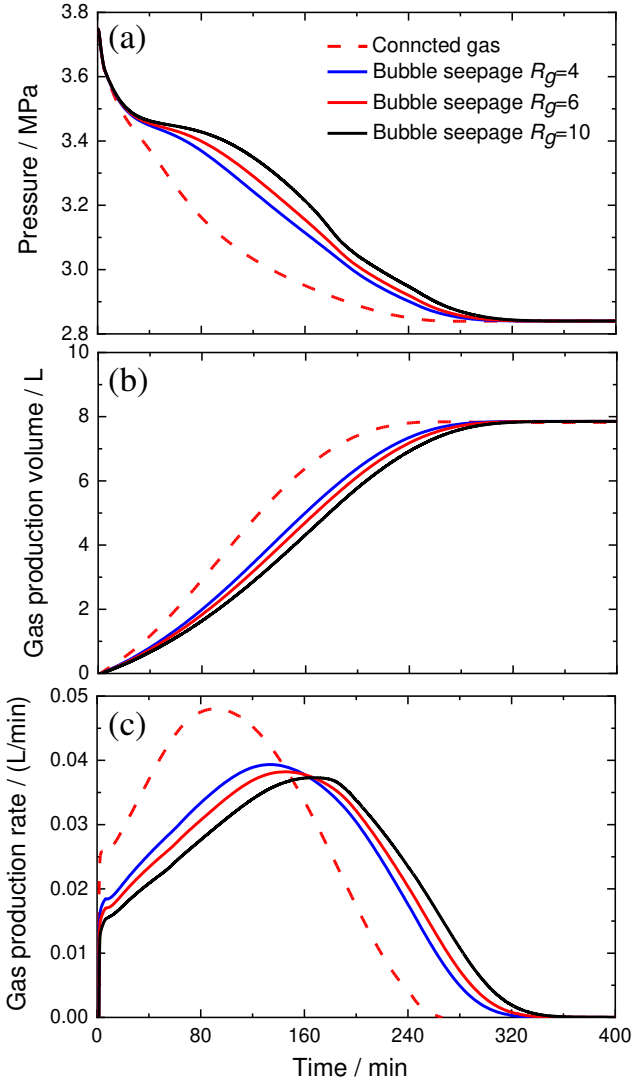

Figure 5. Sensitivity of gas seepage to the maximum flow resistance of isolated bubbles during depressurization-driven hydrate dissociation in water-saturated, low-permeability clayey hydrate-bearing sediments. Variations of (a) pressure, (b) cumulative gas production, and (c) gas production rate during hydrate dissociation.

5 CONCLUSIONS

This paper presents a novel bubble seepage model for characterizing gas migration in hydrate-bearing sediments during hydrate dissociation and gas production. The main findings are summarized as follows.

(1) A modified gas relative permeability function has been introduced to explicitly capture the migration of isolated gas bubbles, connected gas flow, and the transition between these phases.

(2) Validation against experimental data from the dissociation of a field hydrate-bearing sediment demonstrates the model's superior capability in reproducing the pore pressure accumulation phenomena during hydrate dissociation, particularly the pressure accumulation caused by the stagnation of isolated bubble seepage under low gas saturation conditions and the subsequent rapid pressure release upon isolated bubbles merging into connected gas.

(3) Parametric studies reveal that higher bubble flow resistance significantly enhances pore pressure accumulation during initial dissociation stages and delays the timing of peak gas production rates.

ACKNOWLEDGEMENTS

The authors acknowledge the funds from the Natural Science Foundation of China (Nos. 52588202, 52127815).

DATA AVAILABILITY STATEMENT

The data used are available from the corresponding author by request. To be clearly stated in the article.

REFERENCES

Boswell, R. and Collett, T. S. (2011). Current perspectives on gas hydrate resources. *Energy Environ. Sci.*, 4(4): 1206-1215. https://doi.org/10.1039/c0ee00203h

Dai, S., Santamarina, J. C., Waite, W. F. and Kneafsey, T. J. (2012). Hydrate morphology: Physical properties of sands with patchy hydrate saturation. *Journal of Geophysical Research: Solid Earth*, 117: B11205. https://doi.org/10.1029/2012jb009667

Floodgate, G. D. and Judd, A. G. (1992). The origins of shallow gas. *Continental Shelf Research*, 12(10): 1145-1156. https://doi.org/10.1016/0278-4343(92)90075-u

Hu, J., Chen, Y. M., Xu, W. J. and Ke, H. (2024). A bio-hydro-chemical model for gas pressure development in municipal solid waste landfills. *Géotechnique*, 74(7): 647-660. https://doi.org/10.1680/jgeot.21.00306

Ito, T., Komatsu, Y., Fujii, T., Suzuki, K., et al. (2015). Lithological features of hydrate-bearing sediments and their relationship with gas hydrate saturation in the eastern Nankai Trough, Japan. *Marine and Petroleum Geology*, 66: 368-378. https://doi.org/10.1016/j.marpetgeo.2015.02.022

Johnson, A., Patil, S. and Dandekar, A. (2011). Experimental investigation of gas-water relative permeability for gas-hydrate-bearing sediments from the Mount Elbert Gas Hydrate Stratigraphic Test Well, Alaska North Slope. *Marine and Petroleum Geology*, 28(2): 419-426. https://doi.org/10.1016/j.marpetgeo.2009.10.013

Kim, H., Bishnoi, P. R., Heidemann, R. A. and Rizvi, S. S. (1987). Kinetics of methane hydrate decomposition. *Chemical engineering science*, 42(7): 1645-1653.

Kolditz, O., Bauer, S., Bilke, L., Böttcher, N., et al. (2012). OpenGeoSys: an open-source initiative for numerical simulation of thermo-hydro-mechanical/chemical (THM/C) processes in porous media. *Environmental Earth Sciences*, 67(2): 589-599. https://doi.org/10.1007/s12665-012-1546-x

Mahabadi, N., Dai, S., Seol, Y., Sup Yun, T., et al. (2016). The water retention curve and relative permeability for gas production from hydrate-bearing sediments: pore-network model simulation. *Geochemistry, Geophysics, Geosystems*, 17(8): 3099-3110. https://doi.org/10.1002/2016gc006372

Masuda, Y. (1999). Modeling and experimental studies on dissociation of methane gas hydrates in Berea sandstone cores. *Proceedings of the third international gas hydrate conference*.

Milkov, A. V. (2004). Global estimates of hydrate-bound gas in marine sediments: how much is really out there? *Earth-Science Reviews*, 66(3-4): 183-197. https://doi.org/10.1016/j.earscirev.2003.11.002

Olivella, S., Gens, A., Carrera, J. and Alonso, E. (1996). Numerical formulation for a simulator (CODE_BRIGHT) for the coupled analysis of saline media. *Engineering computations*, 13(7): 87-112.

Oshima, M., Suzuki, K., Yoneda, J., Kato, A., et al. (2019). Lithological properties of natural gas hydrate–bearing sediments in pressure-cores recovered from the Krishna–Godavari Basin. *Marine and Petroleum Geology*, 108: 439-470. https://doi.org/10.1016/j.marpetgeo.2019.01.015

Parker, K. M. A. and Mainelli, M. R. (2024). What happens if we 'burn all the carbon'? carbon reserves, carbon budgets, and policy options for governments. *Environmental Science: Atmospheres*, 4(4): 435-454. https://doi.org/10.1039/d3ea00107e

Piñero, E., Marquardt, M., Hensen, C., Haeckel, M., et al. (2013). Estimation of the global inventory of methane hydrates in marine sediments using transfer functions. *Biogeosciences*, 10(2): 959-975. https://doi.org/10.5194/bg-10-959-2013

Ruan, X., Song, Y., Zhao, J., Liang, H., et al. (2012). Numerical Simulation of Methane Production from Hydrates Induced by Different Depressurizing Approaches. *Energies*, 5(2): 438-458. https://doi.org/10.3390/en5020438

Sánchez, M., Santamarina, C., Teymouri, M. and Gai, X. (2018). Coupled Numerical Modeling of Gas Hydrate-Bearing Sediments: From Laboratory to Field-Scale Analyses. *Journal of Geophysical Research: Solid Earth*, 123(12): 2018JB015966. https://doi.org/10.1029/2018jb015966

Santamarina, J. C., Dai, S., Terzariol, M., Jang, J., et al. (2015). Hydro-bio-geomechanical properties of hydrate-bearing sediments from Nankai Trough. *Marine and Petroleum Geology*, 66: 434-450. https://doi.org/10.1016/j.marpetgeo.2015.02.033

Sills, G. C. and Wheeler, S. (1992). The significance of gas for offshore operations. *Continental Shelf Research*, 12(10): 1239-1250. https://doi.org/10.1016/0278-4343(92)90083-V

Sloan, E. D., Jr. (2003). Fundamental principles and applications of natural gas hydrates. *Nature*, 426(6964): 353-363. https://doi.org/10.1038/nature02135

Sultan, N. and Garziglia, S. (2014). Mechanical behaviour of gas-charged fine sediments: model formulation and calibration. *Géotechnique*, 64(11): 851-864. https://doi.org/10.1680/geot.13.P.125

Sun, R. and Duan, Z. (2005). Prediction of CH4 and CO2 hydrate phase equilibrium and cage occupancy from ab initio intermolecular potentials. *Geochimica et Cosmochimica Acta*, 69(18): 4411-4424. https://doi.org/10.1016/j.gca.2005.05.012

Sun, X., Li, Y., Liu, Y. and Song, Y. (2019). The effects of compressibility of natural gas hydrate-bearing sediments on gas production using depressurization. *Energy*, 185: 837-846. https://doi.org/10.1016/j.energy.2019.07.108

Teymouri, M., Sánchez, M. and Santamarina, J. C. (2020). A pseudo-kinetic model to simulate phase changes in gas hydrate bearing sediments. *Marine and Petroleum Geology*, 120: 104519. https://doi.org/10.1016/j.marpetgeo.2020.104519

van der Meer, J. M., Farajzadeh, R., Rossen, W. R. and Jansen, J. D. (2018). Influence of foam on the stability characteristics of immiscible flow in porous media. *Physics of Fluids*, 30(1): 014106. https://doi.org/10.1063/1.5000891

Wang, L., Wang, P., Zhu, B., Kong, D., et al. (2024). Physical Modeling of Hydrate Dissociation in Sandy Sediment by Depressurization under Hypergravity and Normal Gravity Conditions. *Journal of Geotechnical and Geoenvironmental Engineering*, 150(10): 04024096. https://doi.org/10.1061/jggefk.Gteng-11855

Wang, P., Zhu, B., Wang, L., Sun, C., et al. (2025). Enhanced Gas Production via Gas-Driven Fractures during Hydrate Dissociation: Insights from Visualized Experiments. *Energy & Fuels*, 39: 13415-13428. https://doi.org/10.1021/acs.energyfuels.5c01679

Yamamoto, K., Wang, X. X., Tamaki, M. and Suzuki, K. (2019). The second offshore production of methane hydrate in the Nankai Trough and gas production behavior from a heterogeneous methane hydrate reservoir. *RSC Adv*, 9(45): 25987-26013. https://doi.org/10.1039/c9ra00755e

Ye, Z., Wang, L., Zhu, B., Shao, H., et al. (2022). A thermo-hydro-chemo-mechanical coupled model for natural gas hydrate-bearing sediments considering gravity effect. *Journal of Natural Gas Science and Engineering*, 108: 104823. https://doi.org/10.1016/j.jngse.2022.104823

Yun, T. S., Lee, C., Lee, J.-S., Bahk, J. J., et al. (2011). A pressure core based characterization of hydrate-bearing sediments in the Ulleung Basin, Sea of Japan (East Sea). *Journal of Geophysical Research*, 116: B02204. https://doi.org/10.1029/2010jb007468